atmosphere

Article

Intermember Simulation Uncertainty in North Pacific Tropical Cyclone Genesis Frequency Under the Influence of the Interdecadal Pacific Oscillation at Decadal-Scale

Jianing Li [1], Zhen Wang [1,*], Jiuwei Zhao [1], Leying Zhang [2] and Yue Li [1]

[1] School of Atmospheric Sciences, Nanjing University of Information Science and Technology, Nanjing 210044, China; 202312010076@nuist.edu.cn (J.L.); jiuwei@nuist.edu.cn (J.Z.); 202312010075@nuist.edu.cn (Y.L.)
[2] College of Ecology and Environment, Nanjing Forestry University, Nanjing 210037, China; zhangly@njfu.edu.cn
* Correspondence: 202212010012@nuist.edu.cn

Abstract

Substantial uncertainties remain in climate model simulations of tropical cyclones (TCs), particularly those associated with internal climate variability. While the influence of the El Niño–Southern Oscillation (ENSO) on interannual TC variability is well established, the contribution of the Interdecadal Pacific Oscillation (IPO) to decadal-scale uncertainty is less well constrained. Although models generally reproduce IPO-related variations in tropical cyclone genesis frequency (TCGF) over the eastern North Pacific, large discrepancies persist across the broader North Pacific basin. Clarifying the role of IPO in modulating TCGF uncertainty is therefore essential for improving decadal TC projections. In this study, we analyzed a large ensemble of historical simulations from the MRI-AGCM within the d4PDF (Database for Policy Decision Making for Future Climate Change) framework. Empirical orthogonal function (EOF) analysis is applied to IPO-composited fields to identify the leading modes of intermember (100 members *60 y, 6000 times) simulation uncertainty on a decadal-scale. The results reveal that state-of-the-art models exhibit robust and spatially coherent uncertainty structures in TCGF under different IPO phases. Two leading modes are identified: (1) a South China Sea mode, closely associated with systematic precipitation biases, and (2) a zonal dipole mode between the eastern and western North Pacific, linked to the equatorward propagation of Arctic Oscillation (AO)-related variability. Misrepresentation of AO variability is found to contribute substantially to biases in simulated TCGF patterns. Comparisons with observational datasets further support the proposed mechanisms. These findings highlight the importance of improving the representation of precipitation processes and extratropical–tropical teleconnections in climate models, which is critical for enhancing the reliability of decadal predictions of North Pacific TC activity.

Keywords: tropical cyclones; large ensemble simulations; interdecadal pacific oscillation; arctic oscillation; decadal prediction

Academic Editor: Vijay Tallapragada

Received: 16 April 2026
Revised: 3 June 2026
Accepted: 5 June 2026
Published: 12 June 2026

1. Introduction

Tropical cyclone (TC) ranks among the most hazardous weather phenomena on Earth, capable of inflicting severe human and economic losses within hours through extreme rainfall, destructive winds, and storm surges [1–3]. The North Pacific (NP) basin, which accounts for roughly half of the world's annual TC genesis frequency (TCGF), is the most

https://doi.org/10.3390/atmos17060604

active region globally [4]. Located along the western boundary, China, Philippines, South Korea, and Japan bear the brunt of TC impacts, with their vulnerability heightened [5]. Advancing the predictive skill of TC simulations over the NP is fundamental to achieving more accurate forecasts, thereby minimizing disaster-related losses [5,6].

Currently, most state-of-the-art climate models effectively simulate the variability of TC activities [7,8]. However, substantial uncertainties still persist [9–11]. These uncertainties arise from three main sources: scenario uncertainty, model structural uncertainty, and internal climate variability [12–14]. Scenario uncertainty reflects differences in socio-economic development pathways and associated radiative forcing trajectories [15,16]. Model uncertainty is tied to systematic differences in how climate models represent TCGF, intensity, and track behavior [17]. Internal variability, stemming from natural fluctuations, can significantly influence TC behavior at both interannual and interdecadal time scales, such as the El Niño–Southern Oscillation (ENSO) [8,18], Atlantic Multidecadal Oscillation (AMO) [19,20], and Interdecadal Pacific Oscillation (IPO) [21]. The uncertainty caused by the internal atmospheric processes on interannual and interdecadal time scales has not been identified or quantified. This becomes a barrier to improving the reliability of both seasonal prediction and climate projection of TC activities in the NP by climate models.

On an interannual time scale, ENSO modulates the western NP (WNP) TCGF in a southeast–northwest dipole-like pattern [22]. However, climate models exhibit persistent uncertainty in simulating this response. This uncertainty is primarily driven by systematic model biases in amplitude and spatial signatures of ENSO [23], as well as divergent projections of SST warming patterns, which results in conflicting conclusions on the future ENSO–TCGF relationship [24]. Additionally, the challenge of adequately balancing thermodynamic and dynamic feedback has led to poor simulations of multi-year ENSO events poorly simulated in many models [25]. The high sensitivity of “TC seeds” to non-linear warming signals further amplifies the spread in model projections [26]. In addition, Zhao et al. (2023c) [22] found that even given a specific ENSO signal, atmospheric responses can be biased due to errors in simulating tropical precipitation patterns. These biases, which stem from misrepresentations of the Madden–Julian Oscillation and the Pacific–Japan modes, can significantly influence the relationship between ENSO and TCGF.

From decadal to multidecadal time scales, the IPO and AMO modulate SST distributions, large-scale circulation, and convective activity, thereby affecting TCGF, tracks, and intensities [2,8,18]. Compared with the AMO, the IPO exerts a more direct and dominant influence on NP TCGF. As the leading mode of Pacific SST variability, the IPO features a horseshoe-like spatial pattern with ENSO but oscillates on a decadal time scale [27,28]. Over the NP, the TCGF is generally enhanced during the positive IPO phase, as documented by pronounced interdecadal variability in TC activity since the mid-twentieth century [29,30]. Observational and reanalysis studies further indicate that this phase-dependent variability is punctuated by an abrupt reduction in TC activity during the late 1990s, which coincided with a transition of the IPO from a positive to a negative phase around 1997/1998 [29,31,32]. This decline has been widely associated with IPO-related climate variability and is most pronounced over the WNP. In particular, suppressed TCGF over the southeastern WNP accounts for a substantial fraction of the basin-wide reduction and exhibits strong sensitivity to changes in the IPO phase [33].

Significant intermodel spread persists in simulating the TCGF response to IPO-driven decadal variability, highlighting the uncertainty in climate model projections [19,34]. This simulation uncertainty is primarily attributed to model biases in representing the IPO-related tropical Pacific SST gradient and the resulting dynamical environmental responses to this interdecadal forcing [34]. Due to these persistent discrepancies in capturing the IPO signal, biases in atmospheric response can distort the IPO–TCGF relationship, even when forced by observed SST. This underscores the necessity of evaluating models' ability to accurately represent IPO-induced atmospheric signal. In this study, we employ a 100-member historical ensemble from the Database for Policy Decision Making for Future Climate Change (d4PDF) based on MRI-ACGM [35,36], to systematically investigate uncertainties in North Pacific TCGF simulations associated with the IPO and to diagnose the underlying physical mechanisms. We further examine intermember differences in IPO impacts on TCGF, focusing on their connections to basin-scale atmospheric circulation and thermodynamic drivers, with the aim of informing future improvements in decadal prediction capability.

The remainder of this paper is structured as follows: Section 2 outlines the datasets and methods; Section 3 describes the characteristics of IPO-related uncertainties in TCGF; Section 4 explores the associated physical mechanisms; and Section 5 summarizes the main findings and implications.

2. Materials and Methods

2.1. Observational Data

In this study, the observational TC records from 1951 to 2010 are taken from the International Best Track Archive for Climate Stewardship (IBTrACS) [37]. This dataset provides 6-hourly TC positions (latitude and longitude) and intensities (surface wind speed). TC genesis is defined as the first instance when the maximum sustained wind speed reaches 35 knots [37].

Atmospheric reanalyses are sourced from the NCEP (National Centers for Environmental Prediction)/NCAR (National Center for Atmospheric Research) Reanalysis 1 dataset [38]. This dataset provides monthly mean atmospheric fields from 1951 to 2010, including sea level pressure (SLP) and wind fields at 850 hPa and 200 hPa, with a horizontal resolution of 2.5°. Sea surface temperature (SST) data are derived from the NOAA (National Oceanic and Atmospheric Administration) Extended Reconstructed SST (ERSST) v5 dataset [39], and monthly precipitation data are obtained from the NOAA Physical Sciences Laboratory.

We also utilize the ERSSTv5 dataset to define the Interdecadal Pacific Oscillation (IPO) index. The IPO index [28] is constructed based on the difference between SST anomalies (SSTA) in the central equatorial Pacific region (10° S–10° N, 170° E–90° W) and the average of SSTAs in the Northwest Pacific (25° N–45° N, 140° E–145° W) and Southwest Pacific (50° S–15° S, 150° E–160° W). Specifically, we calculate the June–November (JJASON) mean IPO index from 1951 to 2010. The Arctic Oscillation (AO) index is obtained from the NOAA Climate Prediction Center (CPC) (https://www.cpc.ncep.noaa.gov/products/precip/CWlink/daily_ao_index/ao.loading.shtml) (accessed on 1 June 2024).

2.2. Model Data

The model data are from the Database for Policy Decision-Making for Future Climate (d4PDF) project, which is generated using the MRI-AGCM3.2 atmospheric general circulation model [17] developed by the Meteorological Research Institute (MRI), Japan. The d4PDF dataset includes ensemble simulations with 100 members for the period from 1951 to 2010.

MRI-AGCM3.2 features a horizontal resolution of approximately 60 km with 29 vertical levels, allowing it to resolve TC-like vortices [21]. Notably, the model incorporates an advanced cumulus convection scheme, which significantly improves its performance in simulating TCGF climatology [17]. The model is driven by observed daily SST and sea ice data from NOAA, with anthropogenic forcing derived from CMIP5 historical simulations. A key advancement of MRI-AGCM is its large ensemble design that the 100 members share the same observed SST and sea ice conditions, differing only in small perturbations in initial atmospheric states and lateral boundary conditions [10]. This high-resolution dataset with a large ensemble size captures the thermodynamic and dynamic conditions conducive to TC genesis. The data are filtered to remove long-term variability. The model's high resolution enhances the representation of TC genesis processes, while the large ensemble suppresses the randomness of internal process, improving the robustness of the simulations. Moreover, the long temporal span of d4PDF supports research into decadal variability and its relation to climate modes. Additionally, simulations from leading international modeling centers including ECMWF, EC-Earth2, MPI, FGOALS, HadGEM, and NICAM [40–45] were utilized to support this study (Supplementary Table S1). Note that except for the multi-model comparison presented in Figure 1b, all subsequent multi-member ensemble analyses and figures in this study are based exclusively on the 100 ensemble members of the MRI-AGCM.

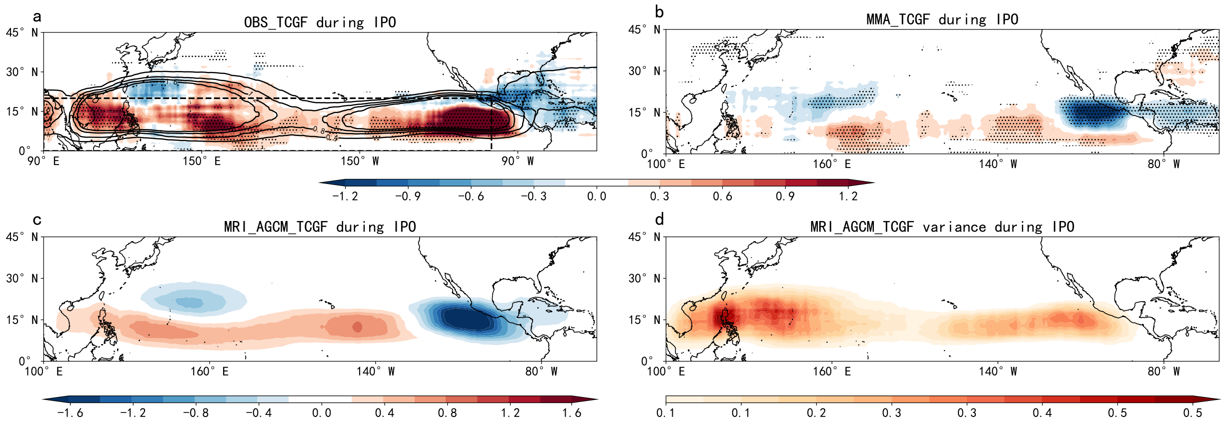

Figure 1. Uncertainty in the simulated TCGF during IPO over the NP. (**a**) Distribution of TCGF anomalies between positive and negative IPO phases based on the observation, with black contours indicating the observed TCGF distribution during the IPO composite years; (**b**) Same as (**a**), but showing the multi-model ensemble mean results from six models: ECMWF, EC-Earth2, MPI, FGOALS, HadGEM, and NICAM; (**c**) same as (**a**), but showing the ensemble mean of 100 members from MRI-AGCM model for d4PDF; (**d**) deviation distribution of the MRI-AGCM ensemble mean simulation (100 members) relative to the result in (**c**). The dashed box in (**a**) indicates the primary study area, the NP.

2.3. Data Extraction and Selection

The algorithm used to detect and extract TCs from the model output is similar to the GFDL tracker (https://www.gfdl.noaa.gov/tstorms/) (accessed on 1 June 2024) and is compatible with the model data used in this study, which is also revealed in previous studies [9,46]. The basic extraction criteria are as follows: (1) Low-pressure center: A surface low-pressure center must be identified. In early TC development, the system may be asymmetric and lack closed isobars. (2) Wind speed and vorticity: The 850 hPa wind speed must exceed 17 $m \cdot s^{-1}$, and the absolute value of the relative vorticity must be greater than 5×10^{-5} s^{-1}. (3) Warm-core structure: The temperature within 1200 km of the TC center must be higher in the 300–500 hPa layer compared to the surrounding 1200–2400 km range to confirm the presence of a warm core. (4) Lifecycle duration: The TC must persist for at least 1.5 days.

We note that although the model TC detection threshold [47] (17 m s^{-1}) and the IBTrACS observation threshold (35 knots, ~18 m s^{-1}) exhibit a minor discrepancy of ~1 m s^{-1}, but this study primarily addresses the large-scale spatial anomaly patterns and intermember variance structures under IPO modulations, rather than absolute TC genesis counts. However, while this subtle threshold difference appears to be small, its potential downstream effects warrant further verification through systematic sensitivity experiments in future work.

In this study, we use TCGF as a proxy for typhoon activity. We count the number of TCs forming within a zonal span of 20° and meridional span of 10° centered at each grid point, with a grid spacing of 1°, ensuring spatial smoothing [19,48]. The selected 20° × 10° box size is motivated by the spatial scale of atmospheric disturbances such as equatorial Rossby waves, mixed Rossby–gravity waves, easterly waves, and other tropical perturbations, which have meridional scales around 2000 km and zonal decay characteristics [49].

2.4. Empirical Orthogonal Function (EOF)

To isolate IPO-related interdecadal variability in TCGF, all time series were first low-pass filtered to retain periods longer than 10 y. The relationships between climate indices and TCGF were quantified using correlation and linear regression. IPO modulation of TCGF was further assessed by compositing anomalies during positive and negative IPO phases, with the composite difference defined as:

$$D_{m,t}(\mathrm{r}) = X^{+}_{m,t}(\mathrm{r}) - X^{-}_{m,t}(\mathrm{r}), \tag{1}$$

where $D_{m,t}(\mathrm{r})$ is the IPO composite-difference field at spatial location r for year t in the m-th ensemble member; $X^{+}_{m,t}(\mathrm{r})$ and $X^{-}_{m,t}(\mathrm{r})$ denote the anomaly fields in composition of positive and negative IPO phases, respectively; $m = 1, 2, \ldots, 100$ is the ensemble-member index; $t = 1, 2, \ldots, 60$ is the year index; and r represents the horizontal grid point over the North Pacific domain. Statistical significance was assessed using a two-tailed Student's t-test at the 95% confidence level.

To diagnose uncertainty in the IPO-related TCGF response, we used the 100-member d4PDF ensemble produced by the MRI-AGCM. EOF analysis was performed over the North Pacific (0–45° N, 100° E–120° W) on the IPO composite-difference fields after reshaping the 100-member, 60-y dataset into 6000 member-year samples. Unlike the conventional EOF approach based on a continuous temporal sequence, this method treats the combined member–year dimension as the sampling space, thereby extracting the dominant spatial structures of uncertainty in the simulated IPO response. The anomaly fields relative to the sample mean were decomposed as:

$$D'_{n}(\mathrm{r}) = \sum_{k=1}^{K} P\,C_k(n)\,EOF_k(\mathrm{r}), \tag{2}$$

Here, $D'_{n}(\mathrm{r})$ is the anomaly field of the n-th sample after removal of the sample mean; $n = 1, 2, \ldots, 6000$ indexes the reshaped member-year samples; $EOF_k(\mathrm{r})$ is the spatial pattern of the k-th EOF mode at location r; $PC_k(n)$ is the corresponding principal component of the k-th mode for the n-th sample; $k = 1, 2, \ldots, K$ is the mode index; and K is the total number of retained EOF modes. Following Zhao (2023) [22], this approach provides a robust estimate of coherent uncertainty patterns across the ensemble. The common structures among samples represent the robust IPO-related response, whereas their spread reflects uncertainty associated with internal atmospheric variability. The first two leading modes were further interpreted by regressing atmospheric circulation fields onto the corresponding principal components.

2.5. Wave Activity Flux Analysis

The wave activity flux (WAF) was computed following Takaya and Nakamura [50]:

$$\begin{aligned} WAF &\\ = \frac{p\ cos\phi}{2|\mathbf{U}|} &\begin{pmatrix} \frac{U}{a^2cos^2\phi}\left[\left(\frac{\partial\psi'}{\partial\lambda}\right)^2 - \psi'\frac{\partial^2\psi'}{\partial\lambda^2}\right] + \frac{V}{a^2cos\phi}\left[\frac{\partial\psi'}{\partial\lambda}\frac{\partial\psi'}{\partial\phi} - \psi'\frac{\partial^2\psi'}{\partial\lambda\partial\phi}\right] \\ \\ \frac{U}{a^2cos\phi}\left[\frac{\partial\psi'}{\partial\lambda}\frac{\partial\psi'}{\partial\phi} - \psi'\frac{\partial^2\psi'}{\partial\lambda\partial\phi}\right] + \frac{V}{a^2}\left[\left(\frac{\partial\psi'}{\partial\phi}\right)^2 - \psi'\frac{\partial^2\psi'}{\partial\phi^2}\right] \end{pmatrix} \end{aligned} \tag{3}$$

Here, U and V denote the climatological zonal and meridional winds at 850 hPa, averaged across the 100 ensemble members. ∣U∣ denotes the magnitude of the climatological horizontal basic flow, which is defined as ∣U∣ = $\sqrt{U^2+V^2}$ (with U and V representing the climatological zonal and meridional wind components, respectively). The stream-function anomaly (ψ') was obtained by regressing the field onto the principal component time series of the leading *EOF* mode. The symbols a, ϕ, and λ represent the Earth's radius, latitude, and longitude, respectively, and p is the pressure at 1000 hPa. The perturbation stream-function (ψ') was derived from the model-simulated anomalous horizontal wind fields (u′ and v′) to avoid the quasi-geostrophic approximation based on geopotential height. Specifically, the anomalous relative vorticity (ζ') was first calculated from the wind components:

$$\zeta' = \frac{\partial v'}{\partial x} - \frac{\partial u'}{\partial y}, \tag{4}$$

Then, the perturbation stream-function was obtained by solving the Poisson equation:

$$\nabla^2\psi' = \zeta', \tag{5}$$

under global boundaries using the standard numerical relaxation method.

3. Results

3.1. Observed and Simulated TCGF Distributions over the NP

By comparing the IPO-composite TCGF distribution over the NP among observations, the MRI-AGCM, and multi-model ensemble means (Figure 1a–c), we derived the multi-member simulation uncertainty in Figure 1d, which constitutes the primary focus of this study. Figure 1a presents the observed TCGF difference between positive and negative IPO phases. During the positive IPO phase, the TCGF anomaly over the NP shows a basin-uniform increase elongated from South China Sea to the Eastern NP despite a slight decrease over extra-tropics in the WNP. This means that the IPO could modulate the whole NP TCGF with uniform TCGF change. The multi-model ensemble mean of TCGF from six high-resolution models reproduces a consistent increase from 150° E to 120° W and a slight decrease over extra-tropics in the WNP (Figure 1b). The TCGF anomalies between positive and negative IPO phases derived from the average of 100 ensemble members in the d4PDF show good consistency with the multi-model ensemble mean (Figure 1b vs. Figure 1c). This suggests that high-resolution models, including d4PDF, demonstrate a reasonable degree of reliability in simulating TC genesis patterns. Moreover, the consistent results between the d4PDF and high-resolution models further confirm that the reliability of d4PDF is not merely due to its own physical parameterizations.

However, discrepancies between observations and simulations still exist. One notable discrepancy between the observed and simulated TCGF responses is located west of California, where the simulated TCGF anomaly exhibits an opposite sign compared to the observations during the positive IPO phase (Figure 1a vs. Figure 1b,c). This could be related to the consistent westward drift of climatology in climate models [45], which is broadly shown in multi-models across six different institutes (Figure 1b) and multi-members of MRI-AGCM (Figure 1c). Here, in this study, we will not extend the analysis of model uncertainty due to the model structure. Instead, we focus on the simulation uncertainty induced by the internal variability of the IPO (Figure 1d). The uncertainty, defined as the standard deviation of TCGF anomalies across 100 members, is shown in Figure 1d. Although the positive IPO contributes to a basin uniform increase of TCGF (Figure 1b,c), it still shows large variability across 100 ensemble members in D4PDF, especially over the

WNP and eastern NP (ENP), indicating strong internal simulation uncertainty under the influence of IPO.

To explore the simulation uncertainty of IPO-related TCGF, we treat simulated TCGF anomalies between positive and negative IPO events as the time dimension across 100 ensemble members and perform EOF analysis (Figure 2). The first EOF mode (EOF1) shows large variability over the South China Sea and weak variability in the ENP (Figure 2a), indicating that the dominant simulation bias is in the WNP. The second EOF mode (EOF2) features a positive anomaly center over the WNP, accompanied by a slight negative anomaly in the South China sea and stronger anomaly the ENP (Figure 2b). These two leading EOF modes together explain 21.7% of the total variance in the TCGF differences simulated under IPO events. Specifically, the EOF1 accounts for 12.2% of the total variance and the EOF2 explains an additional 9.5%.

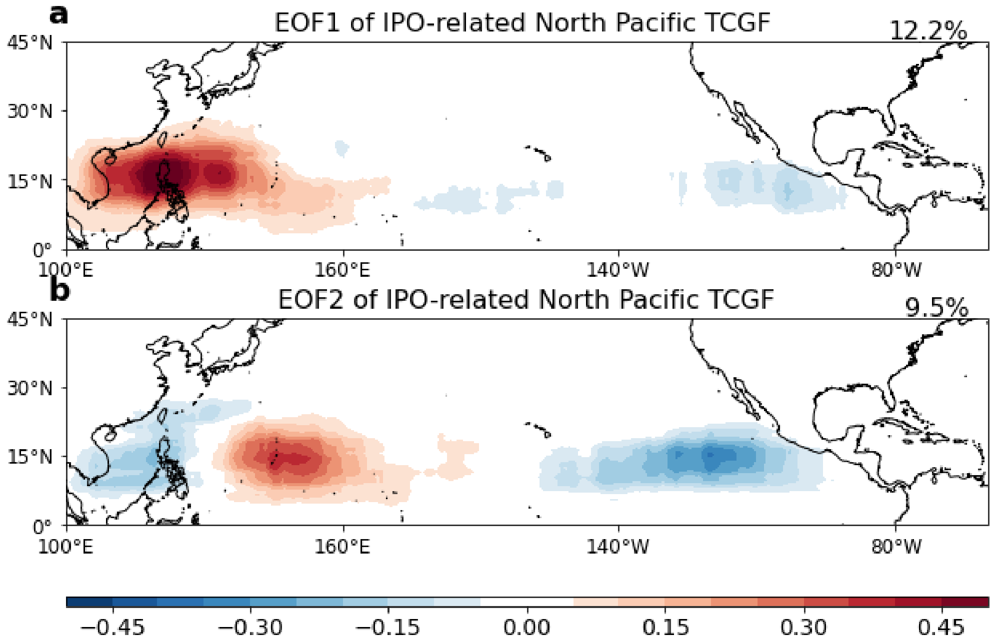

Figure 2. Two EOF modes contributing to the simulation uncertainty of TCGF under IPO impact of NP. (**a**) The first EOF mode of TCGF anomalies between positive and negative IPO phases across 100 ensemble members; (**b**) same as (**a**) but showing the second EOF mode. Here, the TCGF anomalies are obtained from the difference between positive and negative IPO phases. The EOF analysis uses combined members and years (100 members * 60 y) as the temporal dimension and grid cells as spatial variables, with spatial patterns representing the simulation uncertainty.

These findings suggest that while the model ensemble generally captures the spatial pattern of TCGF variability associated with IPO phases (Figure 1), regional uncertainties remain (Figure 2). Based on the spatial distribution of these TCGF anomalies, we identify two distinct modes of simulation uncertainty: the South China Sea mode, characterized by localized variance within the South China Sea (Figure 2a) and the WNP–ENP dipole mode, whereas the response in the South China Sea remains relatively weak in comparison (Figure 2b), which needs to be evaluated when interpreting results from climate model simulations.

Although the explained variance of EOF1 (12.2%) and EOF2 (9.5%) is relatively low due to the immense degrees of freedom in our large-ensemble dataset (100 members $*$ 60 y), both modes are statistically well-separated from higher-order noise (Figure S1). Therefore, while interpretations based on EOF1 should be treated with appropriate caution, these leading modes remain robust and meaningful for capturing the dominant patterns of simulation uncertainty.

3.2. Atmospheric Circulation Patterns Associated with the Two Uncertainty Modes

To further explore what leads to the simulation uncertainty as shown in Figure 2, we regress SLP, upper- and low-level winds onto the two PCs (Figure 3). Figure 3 shows the atmospheric circulation patterns associated with the two leading EOF modes of IPO-related TCGF uncertainty. Figure 3a shows a strong divergent wind field in the upper troposphere over the South China Sea, accompanied by a cyclonic circulation center in the lower troposphere (Figure 3b), positive precipitation anomalies (Figure 3b), and negative SLP anomalies (Figure 3c). This circulation pattern shows a typical baroclinic structure [51,52] over the South China Sea, favorable for tropical cyclone formation. The pronounced precipitation anomaly is likely a key contributor to the uncertainty represented by the first mode.

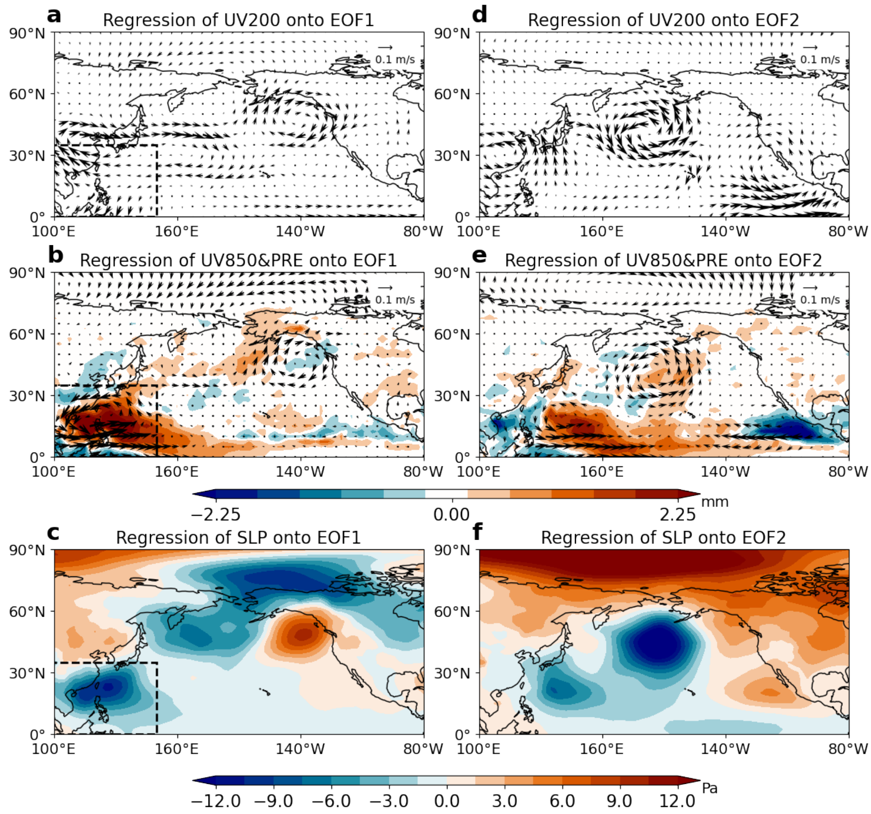

Figure 3. Two modes responsible for the uncertainty in the simulated NP TCGF response to IPO derived from the MRI–AGCM ensemble members. (**a**) 200 hPa wind field (vectors; m s^{-1}) regressed onto the PC1 derived from TCGF differences between positive and negative IPO events (with 100 ensemble members treated as temporal samples); (**b**) Same as (**a**), but for 850 hPa; (**c**) SLP anomaly (shading; Pa) regressed onto the PC1 time series. The dashed rectangles in (**a**–**c**) mark the South China Sea region (0–35° N, 90–150° E). (**d**–**f**) Same as (**a**–**c**), but regressed onto the PC2. In (**a**–**e**), "UV" strictly denotes the horizontal wind vector.

Figure 3d–f display the regressed circulation anomalies onto PC2 of the EOF2. The upper and lower-level circulations exhibit a barotropic structure characterized by a cyclonic circulation anomaly (Figure 3d,e), while a pronounced dipole pattern is observed over the tropical WNP and ENP. In particular, a negative SLP anomaly covers the tropical WNP and a positive one occupies the tropical ENP (Figure 3f), both of which are connected to mid-latitude systems. The SLP anomalies over the extra-tropics compose an Arctic Oscillation (AO)-like pattern, which indicates that the AO could contribute to the simulation uncertainty of the dipole-like change of TCGF in the WNP and ENP (Figure 3f). Next, we explore the roles of precipitation and the AO-like pattern on the TCGF simulation uncertainty of the two modes, respectively.

3.3. Mechanisms Underlying the Two Modes of Uncertainty in TCGF Simulations

3.3.1. The South China Sea Mode

To figure out the coupling relationship between TCGF and precipitation under the influence of the IPO, Figure 4a,b investigate their respective EOF1 over the South China Sea (90–150° E, 0–35° N). Both EOF1 modes exhibit regionally coherent changes. The TCGF high-anomaly region overlaps notably with the central–northern South China Sea and the area east of the Philippines, which further coincides with the centers of intense precipitation. These are similar to the EOF1 of the TCGF over the NP and its regressed precipitation (Figures 2a and 3b). The high fractions of total variance, accounting for 29.7% for TCGF and 33.0% for precipitation, reveal that the EOF1 effectively captures the dominant variability of both TCGF and precipitation. This highlights a robust qualitative spatial consistency between TCGF and precipitation under the modulation of the IPO.

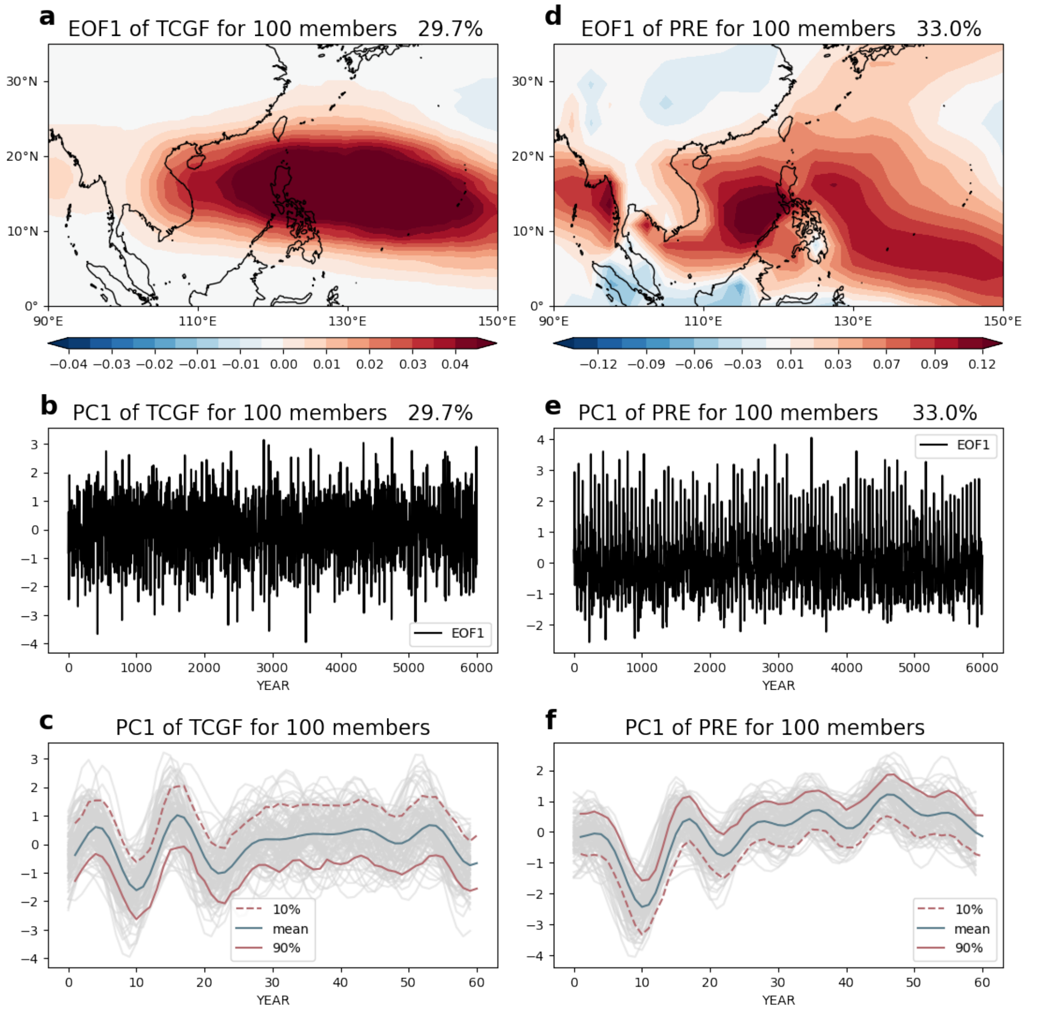

Figure 4. The relationship between TCGF and precipitation of the EOF1. (**a**) First EOF mode of simulated TCGF for the period 1951–2010; (**b**) Time series corresponding to the first EOF mode in (**a**); (**c**) time series after removing the interannual component with the mean (blue line), 90th percentile (solid red line), and 10th percentile (dashed red line) marked; (**d**) first EOF mode of simulated precipitation for the period 1951–2010; (**e**) time series corresponding to the first EOF mode in (**d**); (**f**) same as (**c**), but for the 1951–2010 precipitation time series.

For the TCGF time series, pronounced fluctuations are evident during the first 20 y, followed by relatively smoother variations with small magnitude (Figure 4c). However, the 10th, 90th, and median quantiles across the 100 ensemble members exhibit a substantial spread, reflecting a high degree of intermember divergence and significant inconsistency in the simulated responses, highlighting the large uncertainty in model simulations under the influence of the IPO. The precipitation time series exhibit a general consistency with the TCGF time series, likely associated with enhanced moisture transport driven by the strengthening of the Southwest Monsoon [53]. However, parameterization errors in the model associated with the precipitation process may amplify the uncertainty in TCGF simulation, thereby affecting its spatiotemporal distribution, resulting the uncertainty.

Next, we conduct a quantitative correlation analysis between TCGF and precipitation under the influence of the IPO. To evaluate the statistical relationship, a random sampling analysis was performed (Figure 5), with the samples derived from the MRI-AGCM ensemble-member time series shown in Figure 4c,f. For each sample size, ensemble members were randomly selected without replacement from the 100-member ensemble, and the ensemble-mean precipitation and TCGF indices were subsequently correlated over 10,000 random realizations. The boxplot displays a median correlation coefficient of 0.66 between precipitation and TCGF (Figure 5a), indicating a consistently positive relationship over the South China Sea. While smaller sample sizes (e.g., n = 5 or 10) exhibit a wider dispersion of coefficients and occasional outliers, which underscores the inherent uncertainty in small-sample estimations, the distribution becomes markedly more concentrated as the sample size exceeds 50 (Figure 5b). Specifically, the interquartile range narrows significantly with the median stabilizing between 0.65 and 0.72, demonstrating a clear convergence toward a robust statistical relationship between TCGF and precipitation. The dashed lines denote the critical correlation coefficient threshold of 0.553.

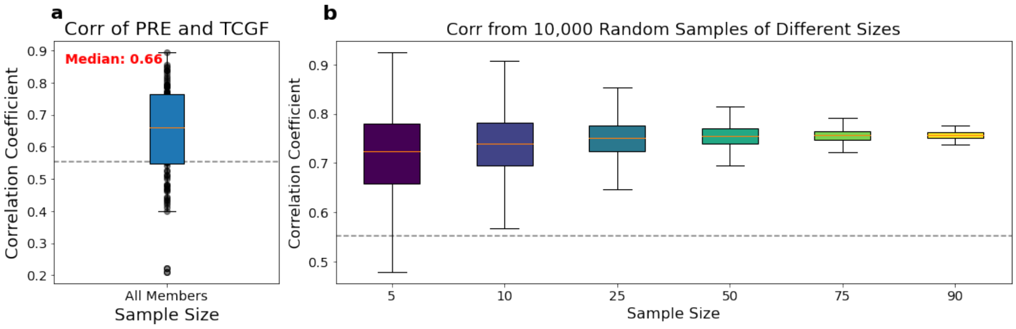

Figure 5. The correlation between precipitation and TCGF from random sampling based on all 100 members of the MRI-AGCM. (**a**) Boxplot of the correlation between precipitation and TCGF for the full sample (unsampled data) and the median is represented by a red line.; (**b**) boxplots of the precipitation–TCGF correlation based on 10,000 random sampling iterations for various sample sizes (n = 5, 10, 25, 50, 75, and 90, with different boxes). The dashed lines indicate a correlation coefficient of 0.553 derived from the 10,000 random subsampling realizations.

After accounting for autocorrelation, the effective degrees of freedom are determined to be 11.302 from Figure S4. For a two-tailed test, the critical correlation coefficient required to pass the 95% confidence level is 0.553. In Figure 5, the values above the dashed lines represent correlation coefficients exceeding this 0.553 threshold. Notably, across both small and large sample sizes, the majority of the sampled correlation coefficients exceed 0.6. This demonstrates that the strong correlation between TCGF and precipitation remains highly robust, even when autocorrelation is strictly taken into account.

Accordingly, results from 10,000 random sampling iterations show that the precipitation–TCGF relationship remains consistently positive as the ensemble sample size increases. Collectively, these findings demonstrate that the strong correlation between precipitation and TCGF (median r = 0.66) is robust within the ensemble framework and exhibits clear convergence behavior across different ensemble sizes.

The physical linkage between precipitation and TCGF over the South China Sea is further investigated through regression analyses of the 850 hPa wind field and SLP onto the PC1 of precipitation EOF1 (Figure 6). During positive precipitation anomalies (Figure 4a), the low-level wind field reveals an anomalous cyclonic circulation over the central South China Sea (Figure 6b,c). The intensified southwesterly monsoon transports moisture northward, where it converges with anomalous easterlies from the north, thereby enhancing convective precipitation. This circulation pattern is highly consistent with the negative SLP anomalies shown in Figure 6c, reflecting the large-scale environmental conditions favorable for TC genesis (Figure 6d). These regression results demonstrate that spatial biases in precipitation simulations are a major source of uncertainty in TCGF simulations.

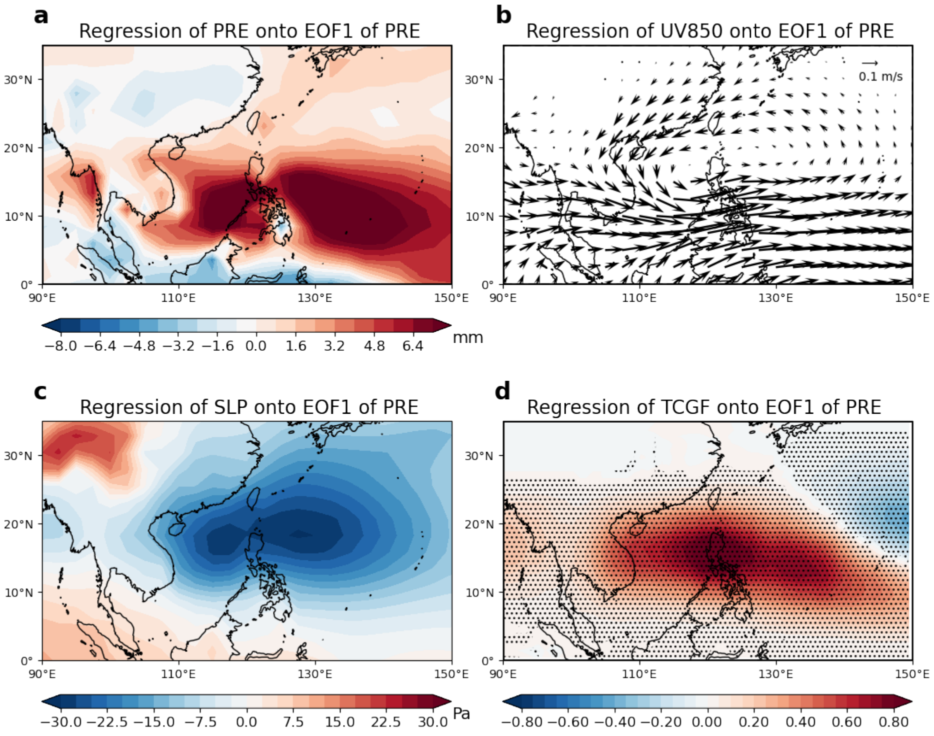

Figure 6. The effect of the first EOF mode of precipitation derived from the MRI–AGCM ensemble members. (**a**) Regression of 850 hPa precipitation onto the first EOF mode time series of model precipitation between positive and negative IPO events; (**b**) same as (**a**), but for 850 hPa wind field, "UV" strictly denotes the horizontal wind vector; (**c**) same as (**a**), but for SLP; (**d**) same as (**a**), but for TCGF (shaded areas indicate significance at the 95% confidence level).

Subsequently, we investigated whether the TCGF uncertainty due to precipitation in the model originates from the IPO. Figure 7 presents the correlation between the IPO and regionally averaged precipitation over the South China Sea during JJASON, derived from both observations (Figure 7a,b) and model simulations (Figure 7c). The observational time series of precipitation and the IPO index, presented before and after removing the linear trend (Figure 7a,b), reveal a clear negative correlation, which becomes more pronounced after detrending. In contrast, model simulations (Figure 7c) yield a weak yet non-negligible positive correlation between the IPO and precipitation. This discrepancy highlights model deficiencies in presenting precipitation responses to IPO forcing. Specifically, uncertainty arises in the model's simulation of precipitation under IPO forcing. This uncertainty subsequently propagates to the TCGF simulation, leading to uncertainty in the modeled TCGF.

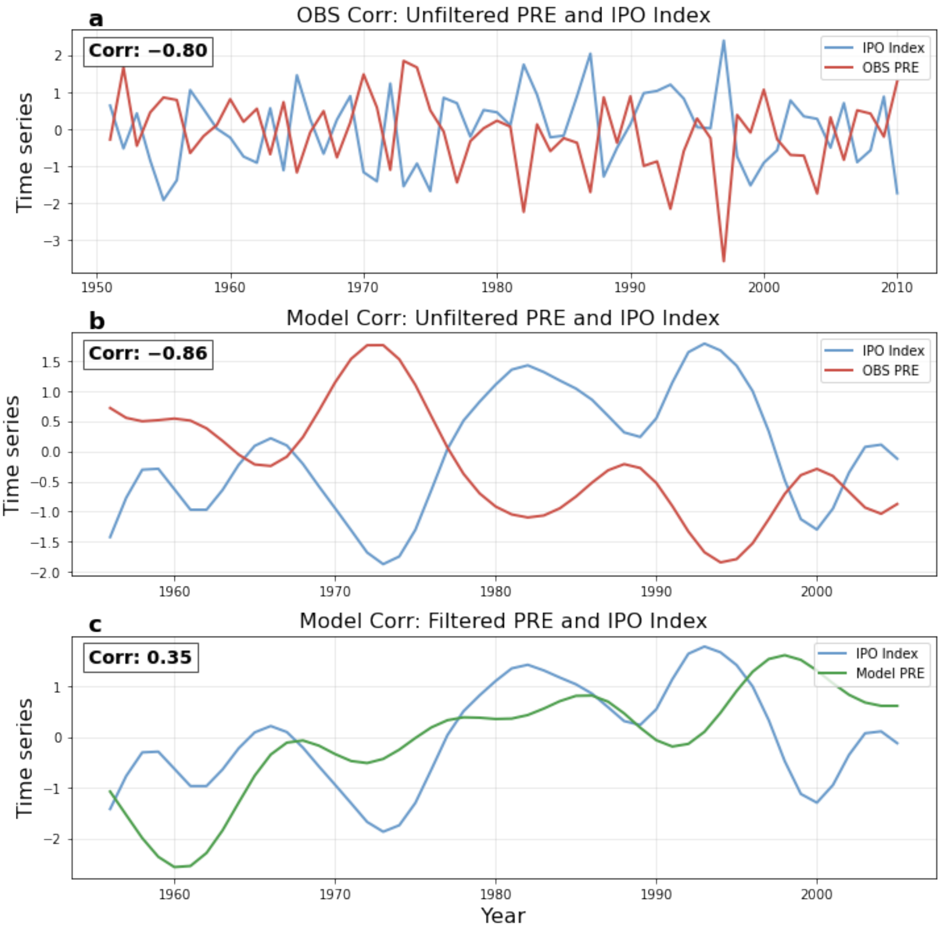

Figure 7. Contrast between observation and MRI–AGCM model simulation over the correlation of IPO and precipitation. (**a**) Linear correlation plot (1951–2010) between the regionally averaged precipitation PCs and the IPO index during JJASON (June–November), derived from observed unfiltered data. (**b**) As in (**a**), but using standardized and low-pass filtered model data to isolate interdecadal variability. (**c**) As in (**b**), but showing the linear correlation derived from the low-pass filtered model simulations.

To understand this bias, we verified that the model reasonably reproduces the climatological mean precipitation distribution over the SCS, suggesting that the deficiency lies in the simulated atmospheric response to decadal SST perturbations rather than the background mean state. Two plausible physical mechanisms may explain this opposite IPO–precipitation relationship. First, the convective parameterization scheme in MRI-AGCM3.2 might exhibit an unrealistic sensitivity to environmental humidity and SST anomalies over the SCS, directly distorting the simulated convective rainfall response [54,55]. Second, the model may misrepresent the responses of the large-scale Walker circulation and low-level moisture convergence to IPO variability over the tropical western Pacific. Since SCS precipitation is strongly regulated by the large-scale overturning circulation and monsoon moisture transport, circulation biases could directly reverse the sign of the simulated precipitation anomalies [27,56]. Although fully isolating the exact process-level origin of this bias is beyond the scope of this study, these factors highlight key simulation uncertainties that warrant further evaluation.

To further assess model performance, we compared precipitation climatology and IPO-related anomalies in observations and simulations (Figure 8). The models reproduce the observed climatological precipitation center over the South China Sea, indicating that they reliably capture the long-term mean precipitation in the absence of IPO forcing (Figure 8a,b). However, the simulated IPO-induced anomalies show an opposing pattern relative to observations (Figure 8b,c vs. Figure 8e,f). Observations indicate suppressed (enhanced) precipitation over the South China Sea during positive (negative) IPO phases, while the model simulates the opposite anomaly sign, while the models simulate positive (negative) anomalies. This contrast underscores substantial uncertainty in simulating IPO-forced precipitation distributions.

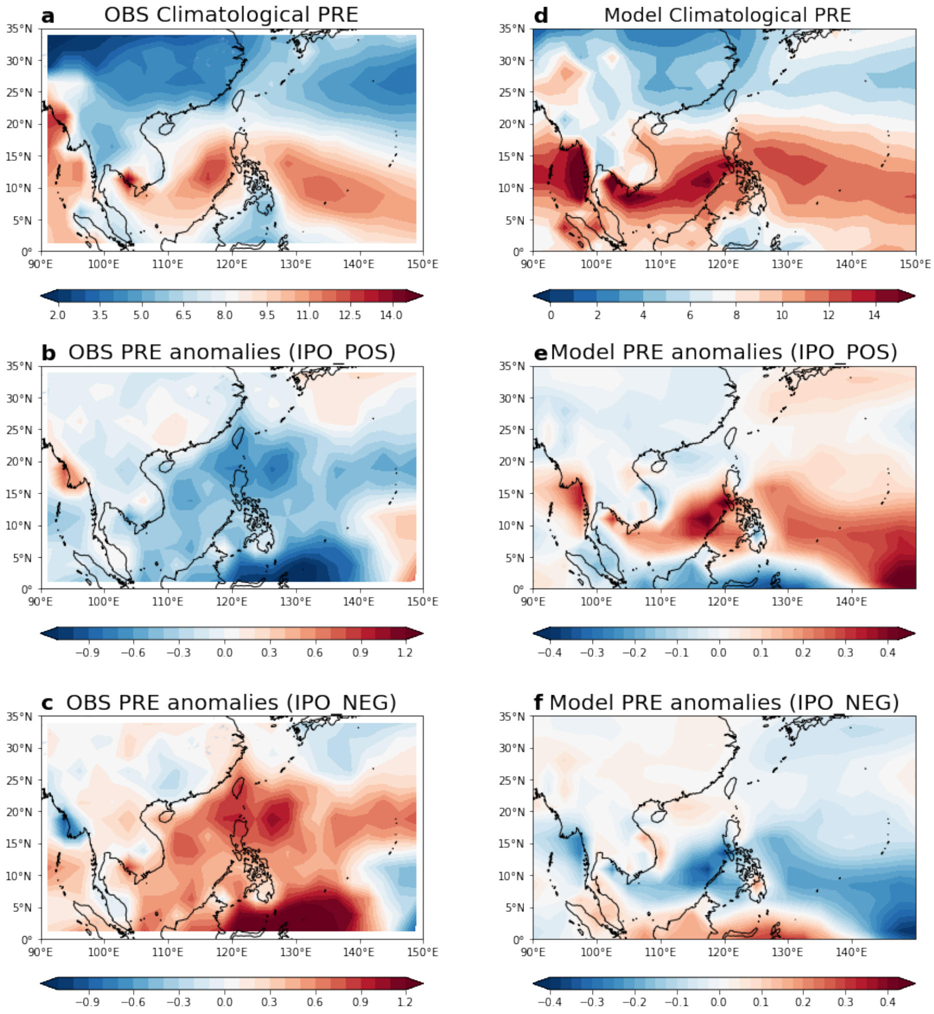

Figure 8. Comparison between observed and model-simulated precipitation responses to the IPO. (**a**) Observational climatological precipitation distribution (1951–2010 mean); (**b**,**c**) composites of observed precipitation anomalies during (**b**) positive and (**c**) negative IPO phases; (**d**–**f**) as in (**a**–**c**), but for model simulations.

Consequently, these results provide robust evidence that the uncertainty in TCGF simulations is intrinsically tied to the model's representation of precipitation responses under IPO forcing. Specifically, compared to observations, the models fail to accurately simulate IPO-induced precipitation; in fact, they produce anomalies that are diametrically opposed to observed patterns. Since precipitation anomalies in the South China Sea are physically coupled with low-level circulation anomalies and SLP variations, this fundamental discrepancy prevents the models from reconstructing the large-scale environments conducive to TC genesis, thereby leading to the significant spatiotemporal biases in simulated TCGF.

3.3.2. The WNP–ENP Dipole Mode

Next, we explore the physical teleconnection between the second mode of TCGF uncertainty and the AO pattern. Since the AO is defined as the leading mode of SLP variability [57], we performed an EOF analysis on the SLP data. As shown in Figure 9a, the EOF1 of SLP reveals that the AO pattern is highly consistent with the circulation anomalies regressed onto PC2 of TCGF uncertainty (as seen in Figure 3d–f). This alignment indicates that the uncertainty mode identified in the North Pacific is indeed driven by the AO. Furthermore, the PC1 of SLP in Figure 9b exhibits significant spread among the 100 ensemble members, highlighting substantial intermember uncertainty in the simulation of the AO itself.

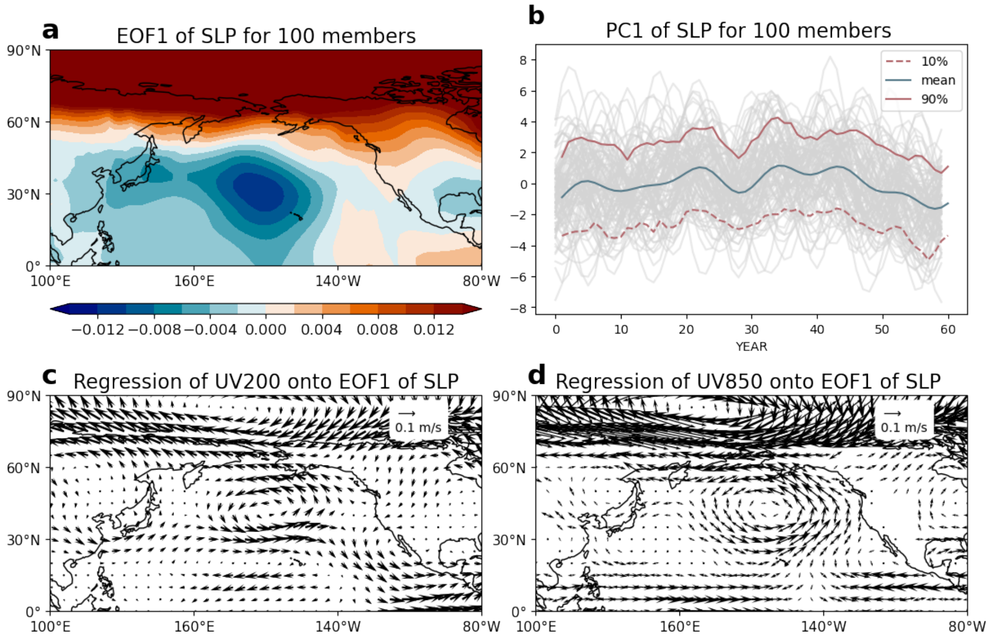

Figure 9. Impact of the AO–induced tropical circulation anomalies on NP. (**a**) Spatial pattern of the first mode of SLP based on IPO phase composites; (**b**) principal component time series of the first mode, showing the ensemble mean (blue line), 10th percentile (red dashed line), and 90th percentile (red solid line); (**c**) regression of 200 hPa wind (horizontal wind direction) field (vectors) onto the time series of the first mode, "UV" strictly denotes the horizontal wind vector; (**d**) regression of 850 hPa wind (horizontal wind direction) field (vectors) onto the time series, "UV" strictly denotes the horizontal wind vector.

To further investigate the impact of this AO-related circulation on the atmospheric environment and TC activity, we regressed the AO time series onto the upper-level and low-level climatological wind fields (Figure 9c,d). During the positive AO phase, a pronounced cyclonic circulation anomaly appears over the mid-to-high latitudes and extends equatorward into the tropics at both levels. However, this equatorward extension exhibits a clear baroclinic structure in the tropics, characterized by easterly wind anomalies at 200 hPa and westerly wind anomalies at 850 hPa over the tropical WNP, with an opposite configuration over the tropical ENP. In the WNP, the coexistence of low-level westerlies and upper-level easterlies leads to a reduction in vertical wind shear and enhances convection activity. Collectively, low-level westerlies typically represent an active convective phase [58–61], these conditions provide a favorable environment for TC genesis in the WNP. In contrast, the ENP exhibits the opposite configuration, creating an environment unfavorable for TC development (Figure 2b).

We next examine how AO-related anomalies in the high latitudes influence tropical circulation. As shown by the climatological wind background in Figure 10a,b, the climatological background meridional wind, collocated with the AO-related cyclonic anomaly, acts as a necessary medium that enables the southward component of the wave group velocity to effectively transport WAF southward. This background flow facilitates the poleward-to-tropical energy transport (Figure 10c), inducing high-latitude circulation anomalies that drive the tropical distribution of TC simulation uncertainty. At 200 hPa, the wave flux propagates equatorward from the AO-related cyclonic anomaly into the tropical region, inducing an anticyclonic circulation anomaly over the WNP and a cyclonic circulation anomaly over the ENP. Accordingly, the associated easterly wind anomaly at 200 hPa over the WNP reduces the local vertical wind shear, favoring TC genesis. In contrast, the westerly wind anomaly over the ENP enhances the vertical wind shear, thereby suppressing TC genesis in that region. Our results indicate that the WNP–ENP dipole mode of TCGF uncertainty is driven by the intermember divergence in AO simulations.

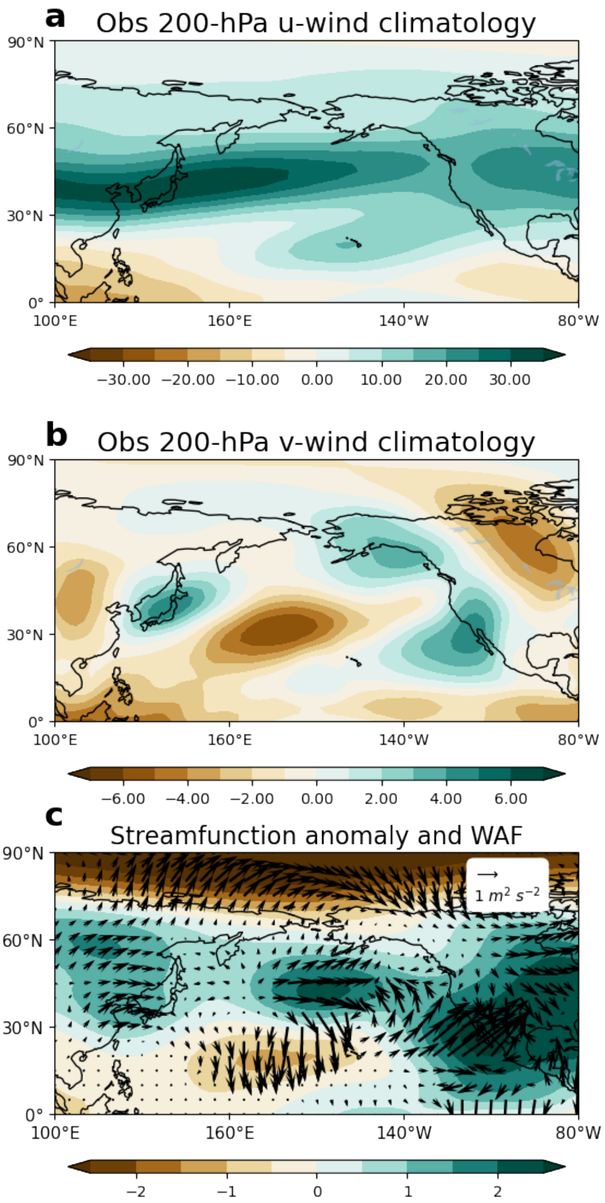

Figure 10. Tropical propagation of AO–induced WAF. (**a**) Observed climatological distribution of 200 hPa zonal wind during JJASON, 1951–2010 (unit: ms^{-1}) from NCEP/NCAR Reanalysis 1 dataset. (**b**) Same as (**a**), but for meridional wind (unit: ms^{-1}); (**c**) distribution of model stream–function anomalies (shading, unit: m^2 s^{-1}) regressed onto the principal component time series of the first EOF mode of model sea level pressure, with vectors indicating WAF from MRI–AGCM model.

This linkage is demonstrated by the prominent AO-like anomalies in the regressed fields of PC2 (Figure 3d–f), which closely resemble the simulated AO pattern (Figure 9a). This relationship is further supported by a high spatial correlation (r = 0.6894, Figure S3) between the two patterns and is validated by observational regressions of the AO onto real-world TCGF (Figure S2). Energy propagates equatorward via WAF, guided by climatological meridional winds. In the tropics, this induces a baroclinic structure: westward propagation in the WNP reduces vertical wind shear, favoring TC genesis, while eastward propagation in the ENP enhances shear, thereby suppressing TC development.

4. Discussion

The findings of this study reveal that TCGF uncertainty under IPO forcing is structured rather than random, emerging through two distinct physical pathways. A critical observation in the South China Sea mode is the discrepancy between the model's ability to simulate climatological mean rainfall and its failure to capture IPO-forced anomalies. This suggests that the uncertainty does not stem from a basic inability to represent tropical convection, but rather from a systematic bias in how the model's convective schemes respond to decadal sea surface temperature (SST) perturbations. Such "response biases" imply that even with perfectly predicted SSTs, the internal atmospheric adjustment remains a major bottleneck for reliable decadal TC projections.

Regarding the WNP–ENP dipole mode, our results underscore the profound influence of extratropical internal variability on tropical TC environments. The significant spread among ensemble members in representing AO circulation, despite sharing identical IPO-related SST forcing, highlights the dominance of internal atmospheric dynamics in shaping regional TCGF uncertainty. This teleconnection, mediated by wave activity flux and guided by the climatological meridional flow, suggests that North Pacific TC activity is not merely a tropical response to local forcing but is also sensitive to the stochastic nature of high-latitude circulation. Consequently, reducing uncertainty in TC projections may require improvements in simulating extratropical–tropical interactions and the fidelity of AO variability within climate models. Previous studies have also highlighted the influence of extratropical circulation variability on WNP tropical cyclone activity. Ho et al. [62] showed that large-scale circulation changes can modulate WNP TC activity on decadal time scales, while Lee et al. [63] emphasized the role of East Asian extratropical circulation variability in regional atmospheric dynamics. These findings support the potential role of AO-related circulation anomalies identified in the present study.

Furthermore, the identification of these two modes places the inherent predictability of decadal TC activity in a new light. The first mode, associated with precipitation response uncertainty over the South China Sea, may partly reflect deficiencies in convective parameterization and large-scale circulation responses to IPO forcing, suggesting that this component of uncertainty could potentially be reduced through model improvement. In contrast, the second mode is more closely linked to AO-related atmospheric internal variability, implying that part of the TCGF uncertainty may arise from intrinsically unpredictable atmospheric fluctuations even under prescribed SST forcing. If a significant portion of TCGF uncertainty is driven by atmospheric internal variability (such as the AO) rather than the ocean-forced response (such as the IPO), it may impose a fundamental limit on the precision of decadal TC outlooks. Future efforts should focus on distinguishing the relative contributions of forced versus internal variability by utilizing even larger ensembles or targeted sensitivity experiments where high-latitude circulation is constrained.

In addition, although MRI-AGCM3.2 at 60 km resolution can represent TC-like vortices, uncertainties associated with TC intensity evolution and track behavior may still affect the identified EOF modes. Nevertheless, the large-scale circulation patterns examined in this study are expected to be more robust than individual TC characteristics.

Nevertheless, some physical coupling may exist, as the AO-related circulation anomalies in EOF2 can modulate low-level moisture transport and monsoon circulation, thereby influencing the South China Sea precipitation associated with EOF1. However, the two modes exhibit distinct spatial structures and dominant mechanisms—EOF1 reflects IPO-modulated regional precipitation uncertainty, while EOF2 captures AO-associated internal circulation and Rossby wave propagation. Therefore, despite potential dynamical interaction, separating these modes remains physically meaningful for isolating the key sources of intermember TCGF simulation uncertainty.

5. Conclusions

By analyzing the 100-member MRI-AGCM historical ensemble based on the MRI-AGCM, this study investigated the uncertainty in North Pacific TCGF under different IPO phases and identified its dominant physical drivers.

The results show that the simulated IPO-related TCGF response contains substantial intermember spread, despite the fact that the ensemble mean broadly reproduces the basin-scale signal. This uncertainty is mainly organized into two leading modes. The first mode is centered over the South China Sea and is primarily associated with uncertainty in the simulated precipitation response to IPO forcing. The second mode exhibits a west–east dipole pattern across the North Pacific and is closely linked to AO-related teleconnections and their influence on tropical circulation.

For the South China Sea mode, the key problem lies in the simulated hydrological response to the IPO. Although models can reproduce the climatological rainfall center, they fail to correctly capture the corresponding precipitation anomalies under IPO forcing. This bias affects sea-level pressure and lower-tropospheric circulation and ultimately leads to large differences in the simulated TCGF response.

For the WNP–ENP dipole mode, the uncertainty mainly arises from intermember divergence in AO circulation anomalies. Wave activity associated with these anomalies propagates equatorward and modifies the upper-level circulation over the tropical Pacific, leading to opposite vertical-wind-shear responses over the WNP and ENP. These circulation differences then produce contrasting TC genesis environments across the basin.

Lastly, the multi-model comparison (including the six high-resolution models and NCEP-NCAR reanalysis) confirms that state-of-the-art AGCMs reasonably capture the observed climatological distribution of North Pacific TCGF. While regional structures of the IPO-forced response vary among models, the MRI-AGCM3.2 ensemble shows a closer spatial agreement with observations and reanalysis than the multi-model ensemble mean. This demonstrates the general reliability of high-resolution climate modeling for TCGF simulations and robustly justifies our selection of the 100-member MRI-AGCM3.2 ensemble as the primary dataset.

Our results on the IPO-modulated North Pacific TCGF align well with previous research showing that the negative IPO suppresses TC genesis via monsoon trough and Walker circulation anomalies [16,33]. However, while most prior studies heavily focused on the WNP or localized regions, the simulation uncertainty of TCGF under the influence of the IPO—especially spanning the entire North Pacific basin—has been less explored. Our study extends these works by using a 100-member ensemble to show that substantial uncertainty exists across the entire basin even without SST differences. Specifically, the identification of the WNP–ENP dipole mode of TCGF uncertainty driven by intermember AO divergence reveals a critical high-to-low latitude teleconnection. This demonstrates that internal atmospheric noise, particularly the simulation accuracy of mid-to-high latitude annular modes like the AO, acts as a primary source of uncertainty when reproducing basin-wide tropical cyclone responses.

Overall, this study shows that the reliability of decadal TCGF simulations depends strongly on how well models represent both IPO-related regional precipitation responses and extratropical–tropical teleconnections. Future improvements may require better representation of convective parameterization processes and more realistic simulation of AO-related large-scale circulation variability. These findings highlight the combined importance of model physics uncertainty and atmospheric internal variability in limiting the reliability of decadal TC projections over the North Pacific. Future improvements in convective parameterization and large-scale circulation simulation may help reduce part of the intermember uncertainty identified in this study.

Supplementary Materials: The following supporting information can be downloaded at: https://www.mdpi.com/article/10.3390/atmos17060604/s1. Figure S1: EOF eigenvalue spectrum (scree plot) of the IPO-composited TCGF differences [22]; Figure S2: Linear regression of observed tropical cyclone genesis frequency (TCGF) anomalies (shading; units: count degree^{-2} year^{-1}) against the observed Arctic Oscillation (AO) index during 1950–2010; Figure S3: Spatial patterns of sea-level pressure (SLP) anomalies (hPa) [27,48–50]; Figure S4: Results of the statistical significance test and autocorrelation diagnostics; Table S1: Comparison of horizontal resolution and ensemble members from different models [21,40–45].

Author Contributions: Conceptualization, J.L. and Z.W.; methodology, J.L., Z.W., J.Z., and L.Z.; validation, J.Z., L.Z., and Y.L.; formal analysis, J.L., J.Z., and L.Z.; investigation, J.L. and Y.L.; data curation, J.L. and Y.L.; visualization, J.L.; writing—original draft preparation, J.L.; writing—review and editing, Z.W., J.Z., L.Z., and Y.L.; supervision, Z.W., J.Z., and L.Z.; project administration, Z.W.; funding acquisition, Z.W. All authors have read and agreed to the published version of the manuscript.

Funding: This research is supported by Open-end Funds of Ministry of Education Key Laboratory for Earth System Modeling (Tsinghua University), Grant Nos. 2211012502701 and 2211012503501.

Institutional Review Board Statement: Not applicable.

Informed Consent Statement: Not applicable.

Data Availability Statement: All datasets utilized in this study can be publicly accessed. The IBTrACS best-track dataset is available at https://www.ncdc.noaa.gov/ibtracs/ (accessed on 1 June 2024); the 6-hourly and monthly reanalysis data of NCEP/NCAR reanalysis can be downloaded from https://psl.noaa.gov/data/gridded/data.ncep.reanalysis.html (accessed on 1 June 2024), respectively; the d4PDF database of the MRI-AGCM for downloading 6-hourly and monthly datasets are available at http://d4pdf.diasjp.net/d4PDF.cgi?target=GCM-subset&lang=en (accessed on 1 June 2024).

Acknowledgments: The authors gratefully acknowledge the support from the School of Atmospheric Sciences, Nanjing University of Information Science and Technology, Nanjing, China, and the College of Ecology and Environment, Nanjing Forestry University, Nanjing, China. The authors also thank colleagues and collaborators for their constructive comments and valuable suggestions.

Conflicts of Interest: The authors declare no conflicts of interest. The funders had no role in the design of the study; in the collection, analyses, or interpretation of data; in the writing of the manuscript; or in the decision to publish the results.

References

1. Zhang, Q.; Wu, L.; Liu, Q. Tropical cyclone damages in China 1983–2006. *Bull. Am. Meteorol. Soc.* **2009**, *90*, 489–496. [CrossRef]
2. Pielke, R.A., Jr.; Gratz, J.; Landsea, C.W.; Collins, D.; Saunders, M.A.; Musulin, R. Normalized hurricane damage in the United States: 1900–2005. *Nat. Hazards Rev.* **2008**, *9*, 29–42. [CrossRef]

3. Swain, D. Tropical Cyclones and Coastal Vulnerability: Assessment and Mitigation. In *Geospatial Technologies for Land and Water Resources Management. Water Science and Technology Library*; Pandey, A., Chowdary, V.M., Behera, M.D., Singh, V.P., Eds.; Springer: Cham, Switzerland, 2022; Volume 103. [CrossRef]
4. Wu, L.; Wang, C.; Wang, B. Westward shift of western North Pacific tropical cyclogenesis. *Geophys. Res. Lett.* **2015**, *42*, 1537–1542. [CrossRef]
5. Emanuel, K. Increasing destructiveness of tropical cyclones over the past 30 years. *Nature* **2005**, *436*, 686–688. [CrossRef]
6. Rogers, R.; Aberson, S.; Black, M.; Black, P.; Cione, J.; Dodge, P.; Dunion, J.; Gamache, J.; Kaplan, J.; Powell, M.; et al. The intensity forecasting experiment: A NOAA multiyear field program for improving tropical cyclone intensity forecasts. *Bull. Am. Meteorol. Soc.* **2006**, *87*, 1523–1538. [CrossRef]
7. Wan, H.; Zhang, S.; Rasch, P.J.; Larson, V.E.; Zeng, X.; Yan, H. Quantifying and attributing time step sensitivities in present-day climate simulations conducted with EAMv1. *Geosci. Model Dev.* **2021**, *14*, 1921–1948. [CrossRef]
8. Zhang, W.; Vecchi, G.A.; Murakami, H.; Villarini, G.; Delworth, T.L.; Yang, X.; Jia, L. Dominant role of Atlantic multidecadal oscillation in the recent decadal changes in western North Pacific tropical cyclone activity. *Geophys. Res. Lett.* **2018**, *45*, 354–362. [CrossRef]
9. Knutson, T.; Camargo, S.J.; Chan, J.C.L.; Emanuel, K.; Ho, C.-H.; Kossin, J.; Mohapatra, M.; Satoh, M.; Sugi, M.; Walsh, K.; et al. Tropical cyclones and climate change assessment. *Bull. Am. Meteorol. Soc.* **2020**, *101*, E303–E322. [CrossRef]
10. Mizuta, R.; Murata, A.; Ishii, M.; Shiogama, H.; Hibino, K.; Mori, N.; Arakawa, O.; Ose, T.; Urabe, Y.; Yoshida, K.; et al. Over 5,000 years of ensemble future climate simulations by 60-km global and 20-km regional atmospheric models. *Bull. Am. Meteorol. Soc.* **2017**, *98*, 1383–1398. [CrossRef]
11. Yoshida, K.; Sugi, M.; Mizuta, R.; Murakami, H.; Ishii, M. Future changes in tropical cyclone activity in high-resolution large-ensemble simulations. *Geophys. Res. Lett.* **2017**, *44*, 9910–9917. [CrossRef]
12. Hawkins, E.; Sutton, R. The potential to narrow uncertainty in regional climate predictions. *Bull. Am. Meteorol. Soc.* **2009**, *90*, 1095–1108. [CrossRef]
13. Zhou, T.; Lu, J.; Zhang, W.; Chen, Z. The sources of uncertainty in the projection of global land monsoon precipitation. *Geophys. Res. Lett.* **2020**, *47*, e2020GL088415. [CrossRef]
14. Wu, M.; Zhou, T.; Li, C.; Li, H.; Chen, X.; Wu, B.; Zhang, L. A very likely weakening of Pacific Walker circulation in constrained near-future projections. *Nat. Commun.* **2021**, *12*, 6502. [CrossRef]
15. Huang, X.; Zhou, T.; Chan, J.C.L.; Zhan, R.; Chen, Z.; Zhao, J. Understanding uncertainties in projections of western North Pacific tropical cyclogenesis. *Environ. Res. Lett.* **2023**, *18*, 114037. [CrossRef]
16. Zhao, J.; Zhan, R.; Wang, Y.; Xie, S.P.; Wu, Q. Untangling impacts of global warming and Interdecadal Pacific Oscillation on long-term variability of North Pacific tropical cyclone track density. *Sci. Adv.* **2020**, *6*, eaba6813. [CrossRef]
17. Murakami, H.; Mizuta, R.; Shindo, E. Future changes in tropical cyclone activity projected by multi-physics and multi-SST ensemble experiments using the 60-km-mesh MRI-AGCM. *Clim. Dyn.* **2012**, *39*, 2569–2584. [CrossRef]
18. Wang, C.; Wang, B.; Wu, L.; Luo, J.J. A dipole variability in tropical cyclone genesis between the western North Pacific and the North Atlantic shaped by Atlantic multidecadal variability. *J. Clim.* **2022**, *35*, 2479–2489. [CrossRef]
19. Song, K.; Zhao, J.; Zhan, R.; Tao, L.; Chen, L. Confidence and uncertainty in simulating tropical cyclone long-term variability using the CMIP6-HighResMIP. *J. Clim.* **2022**, *35*, 6431–6451. [CrossRef]
20. Zhao, J.; Sung, M.K.; Park, J.H.; Luo, J.J.; Kug, J.S. Part I observational study on a new mechanism for North Pacific Oscillation influencing the tropics. *npj Clim. Atmos. Sci.* **2023**, *6*, 15. [CrossRef]
21. Zhao, J.; Sung, M.K.; Park, J.H.; Luo, J.J.; Kug, J.S. Part II model support on a new mechanism for North Pacific Oscillation influence on ENSO. *npj Clim. Atmos. Sci.* **2023**, *6*, 16. [CrossRef]
22. Zhao, J.; Zhan, R.; Murakami, H.; Wang, Y.; Xie, S.-P.; Zhang, L.; Guo, Y. Atmospheric modes fiddling the simulated ENSO impact on tropical cyclone genesis over the Northwest Pacific. *npj Clim. Atmos. Sci.* **2023**, *6*, 213. [CrossRef]
23. Lin, J.; Lee, C.Y.; Camargo, S.J.; Sobel, A. Poleward migration of the latitude of maximum tropical cyclone intensity—Forced or natural? *J. Clim.* **2024**, *37*, 5453–5463. [CrossRef]
24. Xu, M.; Zhan, R.; Zhao, J.; Wang, Y.; Wang, H. Modulation of ENSO–Tropical Cyclone Genesis Frequency Relationship by Sea Surface Warming of Different Spatial Patterns. *J. Clim.* **2026**, *39*, 847–860. [CrossRef]
25. Shi, L.; Hu, S.; Ding, R. Relationship between NPO and multi-year El Niño events in a 2200 years simulation of CESM1. *Clim. Dyn.* **2024**, *62*, 3539–3550. [CrossRef]
26. Xu, M.; Zhan, R.; Zhao, J. Distinct responses of tropical cyclone activity to spatio-uniform and nonuniform SST warming patterns. *Environ. Res. Lett.* **2024**, *19*, 064020. [CrossRef]
27. Dong, B.; Dai, A. The influence of the interdecadal Pacific oscillation on temperature and precipitation over the globe. *Clim. Dyn.* **2015**, *45*, 2667–2681. [CrossRef]
28. Henley, B.J.; Gergis, J.; Karoly, D.J.; Power, S.; Kennedy, J.; Folland, C.K. A tripole index for the interdecadal Pacific oscillation. *Clim. Dyn.* **2015**, *45*, 3077–3090. [CrossRef]

29. Hu, F.; Li, T.; Liu, J.; Bi, M.; Peng, M. Decrease of tropical cyclone genesis frequency in the western North Pacific since 1960s. *Dyn. Atmos. Ocean.* **2018**, *81*, 42–50. [CrossRef]
30. Cao, J.; Feng, J.; Zhao, H.; Wang, B.; Wu, L.; Wang, C. Comparable impacts of IPO and AMO on the decadal change of northern hemisphere tropical cyclone frequency. *Clim. Dyn.* **2025**, *63*, 23. [CrossRef]
31. Hong, C.C.; Wu, Y.K.; Li, T. Influence of climate regime shift on the interdecadal change in tropical cyclone activity over the Pacific Basin during the middle to late 1990s. *Clim. Dyn.* **2016**, *47*, 2587–2600. [CrossRef]
32. Lakshani, W.A.E.; Zhou, W. Observed decadal shifts and trends in global tropical cyclone activities from 1980 to 2021. *Atmos. Ocean. Sci. Lett.* **2023**, *16*, 100321. [CrossRef]
33. Zhao, J.; Zhan, R.; Wang, Y.; Xu, H. Contribution of the interdecadal Pacific oscillation to the recent abrupt decrease in tropical cyclone genesis frequency over the western North Pacific since 1998. *J. Clim.* **2018**, *31*, 8211–8224. [CrossRef]
34. Feng, X.; Wu, L. Roles of interdecadal variability of the western North Pacific monsoon trough in shifting tropical cyclone formation. *Clim. Dyn.* **2022**, *58*, 87–95. [CrossRef]
35. Tiedtke, M. A comprehensive mass flux scheme for cumulus parameterization in large-scale models. *Mon. Weather Rev.* **1989**, *117*, 1779–1800. [CrossRef]
36. Yoshimura, H.; Mizuta, R.; Murakami, H. A spectral cumulus parameterization scheme interpolating between two convective updrafts with semi-Lagrangian calculation of transport by compensatory subsidence. *Mon. Weather Rev.* **2015**, *143*, 597–621. [CrossRef]
37. Knapp, K.R.; Kruk, M.C.; Levinson, D.H.; Diamond, H.J.; Neumann, C.J. The international best track archive for climate stewardship (IBTrACS) unifying tropical cyclone data. *Bull. Am. Meteorol. Soc.* **2010**, *91*, 363–376. [CrossRef]
38. Kalnay, E.; Kanamitsu, M.; Kistler, R.; Collins, W.; Deaven, D.; Gandin, L.; Iredell, M.; Saha, S.; White, G.; Woollen, J.; et al. The NCEP/NCAR 40-Year Reanalysis Project. *Bull. Am. Meteorol. Soc.* **1996**, *77*, 437–472. [CrossRef]
39. Huang, B.; Thorne, P.W.; Banzon, V.F.; Boyer, T.; Chepurin, G.; Lawrimore, J.H.; Menne, M.J.; Smith, T.M.; Vose, R.S.; Zhang, H.-M.; et al. Extended reconstructed sea surface temperature, version 5 (ERSSTv5): Upgrades, validations, and intercomparisons. *J. Clim.* **2017**, *30*, 8179–8205. [CrossRef]
40. Roberts, C.D.; Senan, R.; Molteni, F.; Boussetta, S.; Mayer, M.; Keeley, S.P.E. Climate model configurations of the ECMWF Integrated Forecasting System (ECMWF-IFS cycle 43r1) for HighResMIP. *Geosci. Model Dev.* **2018**, *11*, 3681–3712. [CrossRef]
41. Hazeleger, W.; Wang, X.; Severijns, C.; Ştefănescu, S.; Bintanja, R.; Sterl, A.; Wyser, K.; Semmler, T.; Yang, S.; van den Hurk, B.; et al. EC-Earth V2.2: Description and validation of a new generation Earth system model. *Clim. Dyn.* **2012**, *39*, 2611–2629. [CrossRef]
42. Maher, N.; Milinski, S.; Suarez-Gutierrez, L.; Botzet, M.; Dobrynin, M.; Kornblueh, L.; Kröger, J.; Takano, Y.; Ghosh, R.; Hedemann, C.; et al. The Max Planck Institute Grand Ensemble: Enabling the identification of climate change signals in the presence of internal variability. *Geosci. Model Dev.* **2019**, *12*, 3853–3889. [CrossRef]
43. Li, L.; Yu, Y.; Tang, Y.; Lin, P.; Xie, J.; Song, M.; Dong, L.; Zhou, T.; Liu, H.; Zhu, J.; et al. The flexible global ocean–atmosphere–land system model grid-point version 3 (FGOALS-g3): Description and evaluation. *J. Adv. Model. Earth Syst.* **2020**, *12*, e2019MS002012. [CrossRef]
44. Roberts, M.J.; Baker, A.; Blockley, E.W.; Calvert, D.; Coward, A.; Hewitt, H.T.; Jackson, L.C.; Kuhlbrodt, T.; Mathiot, P.; Roberts, C.D.; et al. Description of the resolution hierarchy of the global coupled HadGEM3-GC3.1 model as used in HighResMIP. *Geosci. Model Dev.* **2019**, *12*, 4999–5028. [CrossRef]
45. Satoh, M.; Tomita, H.; Yashiro, H.; Kajikawa, Y.; Miyamoto, Y.; Yamaura, T.; Miyakawa, T.; Nakano, M.; Kodama, C.; Noda, A.T.; et al. Outcomes and challenges of global high-resolution non-hydrostatic atmospheric simulations using the K computer. *Prog. Earth Planet. Sci.* **2017**, *4*, 13. [CrossRef]
46. Zhao, M.; Held, I.M.; Lin, S.J.; Vecchi, G.A. Simulations of global hurricane climatology, interannual variability, and response to global warming using a 50-km resolution GCM. *J. Clim.* **2009**, *22*, 6653–6678. [CrossRef]
47. Walsh, K.J.E.; Fiorino, M.; Landsea, C.W.; McInnes, K.L. Objectively determined resolution-dependent threshold criteria for the detection of tropical cyclones in climate models and reanalyses. *J. Clim.* **2007**, *20*, 2307–2314. [CrossRef]
48. Lu, M.; Xiong, R. Spatiotemporal profiling of tropical cyclone genesis and favorable environmental conditions in the western Pacific basin. *Geophys. Res. Lett.* **2019**, *46*, 11548–11558. [CrossRef]
49. Chen, G.; Chou, C. Joint contribution of multiple equatorial waves to tropical cyclogenesis over the western North Pacific. *Mon. Weather Rev.* **2014**, *142*, 79–93. [CrossRef]
50. Takaya, K.; Nakamura, H. A formulation of a phase-independent wave-activity flux for stationary and migratory quasigeostrophic eddies on a zonally varying basic flow. *J. Atmos. Sci.* **2001**, *58*, 608–627. [CrossRef]
51. Emanuel, K.A. The maximum intensity of hurricanes. *J. Atmos. Sci.* **1988**, *45*, 1143–1155. [CrossRef]
52. Camargo, S.J.; Emanuel, K.A.; Sobel, A.H. Use of a genesis potential index to diagnose ENSO effects on tropical cyclone genesis. *J. Clim.* **2007**, *20*, 4819–4834. [CrossRef]
53. Wang, B.; Xiang, B.; Lee, J.-Y. Subtropical High predictability establishes a promising way for monsoon and tropical storm predictions. *Proc. Natl. Acad. Sci. USA* **2013**, *110*, 2718–2722. [CrossRef]

54. Del Genio, A.D. Representing the sensitivity of convective cloud systems to tropospheric humidity in general circulation models. *Surv. Geophys.* **2012**, *33*, 637–656. [CrossRef]
55. He, J.; Johnson, N.C.; Vecchi, G.A.; Kirtman, B.; Wittenberg, A.T.; Sturm, S. Precipitation sensitivity to local variations in tropical sea surface temperature. *J. Clim.* **2018**, *31*, 9225–9238. [CrossRef]
56. Meehl, G.A.; Arblaster, J.M.; Fasullo, J.T.; Hu, A.; Trenberth, K.E. Model-based evidence of deep-ocean heat uptake during surface-temperature hiatus periods. *Nat. Clim. Change* **2011**, *1*, 360–364. [CrossRef]
57. Deser, C. On the teleconnectivity of the "Arctic Oscillation". *Geophys. Res. Lett.* **2000**, *27*, 779–782. [CrossRef]
58. Chou, L.C.; Chang, C.P.; Williams, R.T. A numerical simulation of the mei-yu front and the associated low level jet. *Mon. Weather Rev.* **1990**, *118*, 1408–1428. [CrossRef]
59. Kiladis, G.N.; Meehl, G.A.; Weickmann, K.M. Large-scale circulation associated with westerly wind bursts and deep convection over the western equatorial Pacific. *J. Geophys. Res. Atmos.* **1994**, *99*, 18527–18544. [CrossRef]
60. Sperber, K.R. Propagation and the vertical structure of the Madden–Julian oscillation. *Mon. Weather Rev.* **2003**, *131*, 3018–3037. [CrossRef]
61. Cao, X.; Chen, G.-H.; Huang, R.-H.; Chen, W. The intensity variation of the summer intertropical convergence zone in the western North Pacific and its impact on tropical cyclones. *J. Trop. Meteorol.* **2014**, *20*, 193–201. [CrossRef]
62. Ho, C.H.; Baik, J.J.; Kim, J.H.; Gong, D.Y.; Sui, C.H. Interdecadal changes in summertime typhoon tracks. *J. Clim.* **2004**, *17*, 1767–1776. [CrossRef]
63. Lee, J.; Son, S.W.; Cho, H.O.; Kim, J.; Cha, D.H.; Gyakum, J.R.; Chen, D. Extratropical cyclones over East Asia: Climatology, seasonal cycle, and long-term trend. *Clim. Dyn.* **2020**, *54*, 1131–1144. [CrossRef]